

Spin blocker made of semiconductor double quantum well using the Rashba effect

S. Souma¹, H. Mukai¹, M. Ogawa¹, A. Sawada², S. Yokota², Y. Sekine³, M. Eto⁴, and T. Koga²

¹Department of Electrical and Electronics Engineering, Kobe University, Nada, Kobe 657-8501, Japan

²Division of Electronics for Informatics, Graduate School of Information Science and Technology, Hokkaido University, Sapporo, Hokkaido 060-0814, Japan

³NTT Basic Research Laboratories, NTT Corporation, Atsugi, Kanagawa 243-0198, Japan

⁴Faculty of Science and Technology, Keio University, Yokohama 223-8522, Japan

We propose a lateral spin-blockade device that uses an InGaAs/InAlAs double quantum well (DQW), where the values of the Rashba spin-orbit parameter α_R are opposite in sign but equal in magnitude between the constituent quantum wells (QW). By tuning the channel length of DQW and the magnitude of the externally applied in-plane magnetic field, one can block the transmission of one spin (e.g., spin-down) component, leading to a spin-polarized current. Such a spin-blocking effect, brought about by wave vector matching of the spin-split Fermi surfaces between the two QWs, paves the way for a new scheme of spin-polarized electric current generation for future spintronics applications based on semiconductor band engineering.

PACS numbers: 72.25.Dc, 73.63.Hs, 85.75.-d

I. INTRODUCTION

Semiconductor spintronics is a new paradigm for semiconductor electronics which utilizes spins of electrons in addition to charges for device functionalities. Primary areas for potential applications include information storage, computing, and quantum information. One of the pedagogical devices in semiconductor spintronics is the spin field-effect transistor (spin-FET) proposed by Datta and Das,¹ where a spin current injected from the source is controlled by gate via the Rashba spin-orbit interaction (SOI).²⁻⁴ Three elemental technologies are required to realize switching in the spin-FET. The first is the generation and injection of spins into a semiconductor. The second is the manipulation of spins. The third is the detection of spins. Among these mechanisms, the generation of spin-polarized electrons without conventional ferromagnets has certain merits such as efficient spin injection and the absence of stray magnetic fields. While there have been many proposals to fulfill this purpose,^{5,6} the uses of the SOI provide the most popular approaches. These include the intrinsic/extrinsic spin-Hall effect (SHE),⁷⁻¹⁰ spin-filtering devices using resonant tunneling diodes (RTD),¹¹⁻¹³ those utilizing quantum point contact (QPC),¹⁴⁻¹⁷ and topologically protected surface current in topological insulators (TI).^{18,19} While the intrinsic mechanisms (intrinsic SHE and TI) potentially provide an ideal (the most efficient) source for the spin-polarized current, the actual utilization of these are hindered by the lack of their controllability. The extrinsic mechanisms, on the other hand, provide good controllability in the actual devices, whereas the efficiencies of the spin current generation are typically very low.²⁰

In this report, we propose a new spin-filtering device which provides both excellent controllability and efficiency, based on the extrinsic SOI mechanism, utilizing a narrow gap semiconductor double quantum well (DQW) structure.^{12,21-24} In this device, the combination of the Rashba SOI and the external orbital magnetic field en-

ables the perfect blockade of only one spin component, thereby generating a spin-polarized current. Our DQW-based device has advantages over the QPC-based devices in a sense that it is compatible with the conventional lithographic top-down processes and that a large (spin-polarized) current can be extracted from the device.

We organize the paper as follows. We introduce the concept of the proposed device in the next section. This is followed by a description of tight-binding (TB) model that simulates the function of our device (Sec. III), where we also show how the parameter values for the TB model were chosen and that the resultant energy dispersion relation indeed agreed with that of the effective mass model. Section IV is devoted to the discussions of the spin dependent conductance and the spin-filtering effect observed in the proposed device. Our conclusions are given in Sec. V.

II. DEVICE CONCEPT

A. Device description

Figure 1(a)(b) illustrates the proposed spin filtering device based on the DQW structure, where each QW (QW1 and QW2), by itself, has an asymmetric confinement potential. The locally averaged electric fields within QW1 and QW2, necessary for the Rashba SOI for each QW, are denoted as $\langle E_z \rangle_1$ and $\langle E_z \rangle_2$, respectively.²⁵ These electric fields satisfy the relation $\langle E_z \rangle_1 = -\langle E_z \rangle_2 > 0$ by symmetry where the z direction is normal to the sample surface. Such a DQW structure can be realized using (001) InP lattice-matched $\text{In}_{0.53}\text{Ga}_{0.47}\text{As}/\text{In}_{0.52}\text{Al}_{0.48}\text{As}$ material system as will be explained in Sec. IIIB. The thicknesses of QW1 and QW2 are both d_{QW} , which are separated by a barrier layer with thickness d_B . The value of d_B should be so chosen that QW1 and QW2 are only weakly coupled. The active part of the device, composed of DQW, has a length L in the x direction. Non-magnetic electrodes are attached to QW1

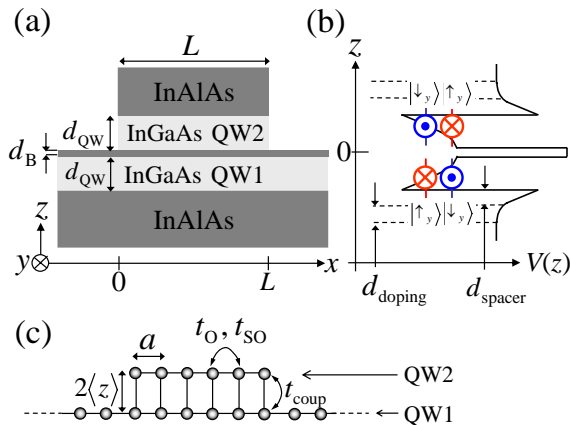


FIG. 1: (a) Schematic illustration of the proposed spin-blocking device made of double quantum well. (b) Sketch of the potential profile in the DQW region with zero magnetic field. The spin-dependent energy eigenvalues for the given wave vector value $\mathbf{k} = (k_F, 0)$ due to the Rashba SOI are also indicated. (c) The equivalent tight-binding lattice model to simulate the transport properties of the electron along \hat{x} .

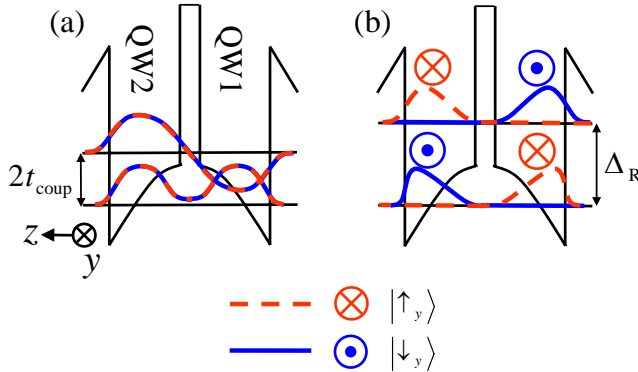


FIG. 2: (Color online) Sketches of electron wave functions along z -direction at $B = 0$. (a) The case without the Rashba SOI or with $\mathbf{k} = (0, 0)$ for the in-plane wave vector, where we obtain the same orbital wave functions irrespective of spins. (b) The case with the Rashba SOI and $\mathbf{k} = (k_F, 0)$. The Rashba splitting Δ_R is assumed to be much larger than the inter-well coupling t_{coup} . While the spin degeneracy is preserved due to the inversion symmetry, the orbital wave functions are not identical between the different spins in each spin degenerate energy level.

of the DQW device at both the left and right ends, between which an electric current is passed through. The width of the device in the y direction is assumed to be much larger than L so that the periodic boundary condition is applicable.

With the DQW structure described in Fig. 1(b), one may encounter the following dilemma. QW1 and QW2

alone are inversionally asymmetric, which supports the presence of the Rashba splitting. However, if one sees the whole DQW as a single quantum mechanical system, it is inversionally symmetric, which is against the presence of the Rashba splitting. Such dilemma is resolved as follows. If one sees QW1 and QW2 as independent quantum wells, the Rashba spin splitting is indeed induced with a finite given wave vector $\mathbf{k} = (k_F, 0)$ in each QW. However, if one sees the DQW as a single quantum mechanical system, what we interpreted as the spin splitting of a single quantum well above is now viewed as a spin degenerate subband splitting derived from a single DQW (see Figs. 2 and 3).

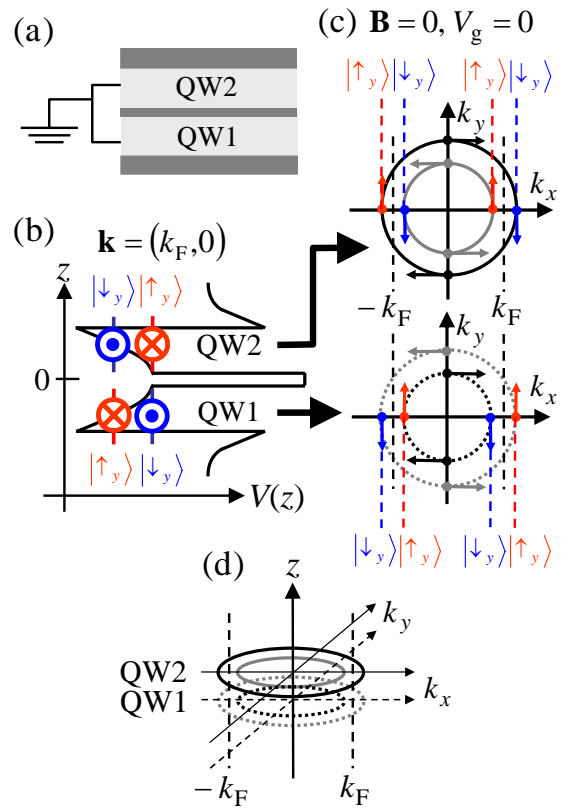


FIG. 3: (Color online) (a) Illustration of unbiased DQW system without magnetic field. (b) A pair of spin degenerate eigenenergies for $\mathbf{k} = (k_F, 0)$ in the DQW. (c) Spin-dependent Fermi circles for independent QW1 and QW2, where indicated by the arrows on the circles are the spin orientations. (d) 3D illustrations of the overlapped Fermi circles of the DQW with the given condition, where the vertical axis is z in the real space.

B. Formation of the bonding and antibonding wave functions for a selected spin by the in-plane magnetic field at the Fermi circle points $(\pm k_F, 0)$

($H = H_0 + H_R + H_Z$) reads

$$H_0 = \frac{\hbar^2}{2m_{||}^*} \left[(k_x + eBz/\hbar)^2 + k_y^2 \right] - \frac{d}{dz} \frac{\hbar^2}{2m_z^*(z)} \frac{d}{dz} + V(z), \quad (1)$$

$$H_R = \alpha(z) [k_y \sigma_x - (k_x + eBz/\hbar) \sigma_y]$$

and

$$H_Z = -\frac{1}{2}g^* \mu_B B \sigma_y,$$

where H_0 , H_R and H_Z are the unperturbed Hamiltonian, Rashba and Zeeman Hamiltonians, respectively, $\mu_B = e\hbar/2m_e$ is the Bohr magneton (m_e being the free electron mass), g^* is the effective g -factor value, $m_{||}^*$ and $m_z^*(z)$ are the in-plane and out-of-plane effective masses, respectively, the latter incorporating different effective mass values for the well and barrier materials. $\mathbf{k} = (k_x, k_y)$ is the in-plane wave vector of an electron.²⁶ e is the elementary charge. \hbar is Planck's constant divided by 2π . σ_x and σ_y are the Pauli spin matrices. For the $\text{In}_{0.53}\text{Ga}_{0.47}\text{As}/\text{In}_{0.52}\text{Al}_{0.48}\text{As}$ material system, we can safely ignore H_Z and eBz/\hbar relative to H_R and k_x , respectively, and so we do hereafter.²⁷

Using the material-dependent intrinsic constant a_{SO} for the Rashba SOI,²⁸ $\alpha(z)$ can be written as $(a_{SO}/e)(\partial V(z)/\partial z)$, where the contributions from the band discontinuities at the well-barrier interfaces are readily included in this formulation and should be excluded in taking the derivative $\partial V(z)/\partial z$. We also define the parameter value α_R by $\langle \Phi_{QW1} | \alpha(z) | \Phi_{QW1} \rangle = a_{SO} \langle E_z \rangle_1$ or equivalently $-\langle \Phi_{QW2} | \alpha(z) | \Phi_{QW2} \rangle = -a_{SO} \langle E_z \rangle_2$, where $|\Phi_{QW1(QW2)}\rangle$ is the energy eigenstate of the independent QW1 (QW2) in the confining direction.

In Eq. (1), we see that applying a magnetic field ($\mathbf{B} \parallel \hat{y}$) has the effect of shifting the Fermi circle in the k_x direction by the magnitude $-eBz/\hbar$. Setting the origin of z at the middle of the barrier layer, the Fermi circles for QW1 and QW2 are shifted oppositely along k_x axis as shown in Fig. 4. We then claim that the spin blocking effect is maximized when the magnitude of the Fermi circle shift becomes equal to the Rashba wave number k_α , where $k_\alpha \equiv m_{||}^* \alpha_R / \hbar^2$. We call the corresponding magnetic field as the “anticrossing” magnetic field $B_{ac} \equiv \hbar k_\alpha / e \langle z \rangle$, where $\langle z \rangle \equiv \langle \Phi_{QW2} | z | \Phi_{QW2} \rangle = -\langle \Phi_{QW1} | z | \Phi_{QW1} \rangle > 0$ (see Fig. 4).

With this condition ($B = B_{ac}$), defining the spin-up direction in \hat{y} and neglecting the interaction between QW1 and QW2, the front and back edges of the Fermi circles for spin-down electrons in the current direction ($\parallel \hat{x}$) are at $\mathbf{k} = (k_F, 0)$ and $(-k_F, 0)$, respectively, for both QW1 and QW2. For spin-up electrons, those of QW1 and QW2 are at $(\pm k_F + 2k_\alpha, 0)$ and $(\pm k_F - 2k_\alpha, 0)$, respectively, as shown in Fig. 4(c). If the interaction between QW1 and QW2 is turned on, only the spin-down electrons form the bonding- and antibonding-like wave functions around the Fermi circle points $(\pm k_F, 0)$ in the presence of $B = B_{ac}$.

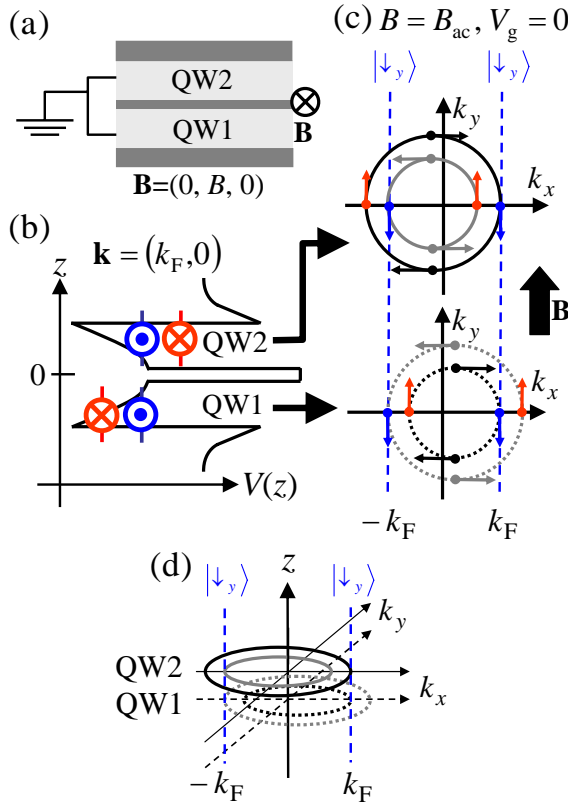


FIG. 4: (Color online) (a) Illustration of unbiased DQW in the presence of the magnetic field $\mathbf{B} = (0, B, 0)$. (b) Spin-dependent eigenenergies in the DQW with $\mathbf{k} = (k_F, 0)$ and $B = B_{ac}$ (see text for B_{ac}). (c) Spin-dependent Fermi circles for independent QW1 and QW2 at $B = B_{ac}$, where we set $z = 0$ at the middle of the center barrier layer. (d) 3D illustration of the overlapped Fermi circles of the DQW with the given condition.

Let us consider the effect of applying an in-plane magnetic field ($\mathbf{B} \parallel \hat{y}$) to the DQW, which provides a key element to the proposed spin-blocking mechanism. Setting $\mathbf{p} \rightarrow \mathbf{p} + e\mathbf{A}$ in the Hamiltonian using the vector potential $\mathbf{A} = (Bz, 0, 0)$, which leads to $\mathbf{B} = \nabla \times \mathbf{A} = (0, B, 0)$, the Hamiltonian of an electron in the DQW

C. Spin-blockade mechanism explained by the spin-selective flying qubit model

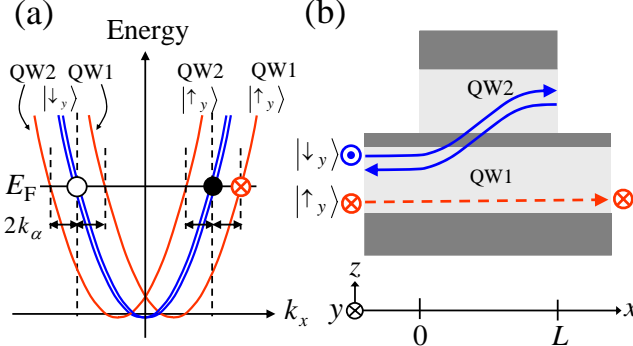


FIG. 5: (Color online) (a) Energy dispersion relation of the proposed DQW when the in-plane magnetic field $\mathbf{B} = (0, B_{\text{ac}}, 0)$ is applied. (b) Spin dependent trajectories of an electron which is injected in QW1 from left, where the Fermi wave number matching condition is satisfied with the in-plane magnetic field $\mathbf{B} = (0, B_{\text{ac}}, 0)$.

Let us consider the Fermi circle points of the DQW on the k_x axis in the presence of $\mathbf{B} = (0, B_{\text{ac}}, 0)$. The k_x values of these points are $-(k_F + 2k_\alpha)$ (spin-up), $-k_F$ (spin-down, doubly degenerate), $-(k_F - 2k_\alpha)$ (spin-up), $k_F - 2k_\alpha$ (spin-up), k_F (spin-down, doubly degenerate), and $k_F + 2k_\alpha$ (spin-up), if the inter-well coupling is neglected. The degeneracies at $\pm k_F$ are lifted if the inter-well coupling is turned on, i.e., $k_F \rightarrow k_F \pm k_{\text{coup}}$ with $k_{\text{coup}} = t_{\text{coup}}(dE(k_x)/dk_x)^{-1}$, where t_{coup} and $E(k_x)$ are a half of the subband splitting energy and the energy dispersion relation of the unperturbed hamiltonian H_0 with $B = 0$, respectively. We note that the states with $\pm k_F - 2k_\alpha$ have a wave function along \hat{z} nearly equal to $|\Phi_{\text{QW}2}\rangle \otimes |\downarrow_y\rangle$, while that for $\pm k_F + 2k_\alpha$ is $|\Phi_{\text{QW}1}\rangle \otimes |\uparrow_y\rangle$. The Fermi circle points $(\pm (k_F + k_{\text{coup}}), 0)$ and $(\pm (k_F - k_{\text{coup}}), 0)$, on the other hand, form bonding- and antibonding-like wave functions between QW1 and QW2, respectively. The superposition of these wave functions causes precessional motion of electron between QW1 and QW2 as we see below.²⁹

Letting $|\Phi_{\text{QW}1}^{\downarrow y}\rangle = |\Phi_{\text{QW}1}\rangle \otimes |\downarrow_y\rangle = {}^t(1, 0) \otimes |\downarrow_y\rangle$ and $|\Phi_{\text{QW}2}^{\downarrow y}\rangle = |\Phi_{\text{QW}2}\rangle \otimes |\downarrow_y\rangle = {}^t(0, 1) \otimes |\downarrow_y\rangle$ be the spin-down wave functions confined in QW1 and QW2, respectively, the bonding- and antibonding-like wave functions, which are the spin-down energy eigenstates at $(\pm (k_F + k_{\text{coup}}), 0)$ and at $(\pm (k_F - k_{\text{coup}}), 0)$ are, respectively,

$$|\Phi_b^{\downarrow y}\rangle = \frac{1}{\sqrt{2}} \begin{pmatrix} 1 \\ 1 \end{pmatrix} \otimes |\downarrow_y\rangle = \frac{1}{\sqrt{2}} (|\Phi_{\text{QW}1}^{\downarrow y}\rangle + |\Phi_{\text{QW}2}^{\downarrow y}\rangle) \quad (2)$$

and

$$|\Phi_a^{\downarrow y}\rangle = \frac{1}{\sqrt{2}} \begin{pmatrix} 1 \\ -1 \end{pmatrix} \otimes |\downarrow_y\rangle = \frac{1}{\sqrt{2}} (|\Phi_{\text{QW}1}^{\downarrow y}\rangle - |\Phi_{\text{QW}2}^{\downarrow y}\rangle). \quad (3)$$

Next, we consider how the wave function $e^{ik_F x} |\Phi_{\text{QW}1}^{\downarrow y}\rangle$ in the left lead of the device propagates through the active part of the DQW device ($0 \leq x \leq L$). At $x = 0$, $|\Phi_{\text{QW}1}^{\downarrow y}\rangle = \frac{1}{\sqrt{2}} (|\Phi_b^{\downarrow y}\rangle + |\Phi_a^{\downarrow y}\rangle)$ from Eqs. (2) and (3), where the plane wave parts for $|\Phi_b^{\downarrow y}\rangle$ and $|\Phi_a^{\downarrow y}\rangle$ are $e^{i(k_F + k_{\text{coup}})x}$ and $e^{i(k_F - k_{\text{coup}})x}$, respectively, at the Fermi energy E_F . Thus, the wave function $e^{ik_F x} |\Phi_{\text{QW}1}^{\downarrow y}\rangle$ in the left lead ($x < 0$) connects to a superpositioned state $|\Psi_{\text{inj}}^{\downarrow y}(x)\rangle \equiv \frac{e^{ik_F x}}{\sqrt{2}} (e^{ik_{\text{coup}} x} |\Phi_b^{\downarrow y}\rangle + e^{-ik_{\text{coup}} x} |\Phi_a^{\downarrow y}\rangle) = e^{ik_F x} \{ \cos(k_{\text{coup}} x) |\Phi_{\text{QW}1}^{\downarrow y}\rangle + i \sin(k_{\text{coup}} x) |\Phi_{\text{QW}2}^{\downarrow y}\rangle \}$ in the DQW ($x \geq 0$) [the point indicated with \bullet in Fig. 5(a)]. This wave function portrays the precessional motion of an spin-down electron between QW1 and QW2 within the DQW, where the condition $L = L_n \equiv (n - \frac{1}{2}) \pi/k_{\text{coup}}$, n being an integer, makes an electron be backscattered at the end of the DQW within QW2. The backscattered wave function $e^{-ik_F(x-L)} |\Phi_{\text{QW}2}^{\downarrow y}\rangle$ at $x = L$ now connects to $\frac{e^{-ik_F x'}}{\sqrt{2}} (e^{-ik_{\text{coup}} x'} |\Phi_b^{\downarrow y}\rangle - e^{ik_{\text{coup}} x'} |\Phi_a^{\downarrow y}\rangle) = e^{-ik_F x'} \{ -i \sin(k_{\text{coup}} x') |\Phi_{\text{QW}1}^{\downarrow y}\rangle + \cos(k_{\text{coup}} x') |\Phi_{\text{QW}2}^{\downarrow y}\rangle \}$ in the DQW [the point indicated with \circ in Fig. 5(a)], where $x' = x - L$, which propagates back to QW1 at $x = 0$ following the trajectory of $|\Psi_{\text{inj}}^{\downarrow y}(x)\rangle$ backward as shown by the arrowed curves marked with \odot in Fig. 5(b).

Electrons with up-spin, on the other hand, injected from the left lead to QW1, are transmitted straight to the right lead, i.e., $|\Psi_{\text{inj}}^{\uparrow y}(x)\rangle \equiv e^{i(k_F + 2k_\alpha)x} |\Phi_{\text{QW}1}^{\uparrow y}\rangle$ as shown by the arrowed broken line in Fig. 5(b).

The probabilities of finding spin-down and spin-up electrons in QW1 at the position $x = L$ upon injecting the same spin in QW1 at position $x = 0$ are given naively as

$$T_{\uparrow(\text{QW}1)} = \left| \langle \Phi_{\text{QW}1}^{\uparrow y} | \Psi_{\text{inj}}^{\uparrow y}(L) \rangle \right|^2 = 1, \quad (4)$$

and

$$T_{\downarrow(\text{QW}1)} = \left| \langle \Phi_{\text{QW}1}^{\downarrow y} | \Psi_{\text{inj}}^{\downarrow y}(L) \rangle \right|^2 = \cos^2(k_{\text{coup}} L) \quad (5)$$

respectively. This means that the transmission probability of spin-down electron oscillates with the device length L , while that of spin-up electron is not (always unity).

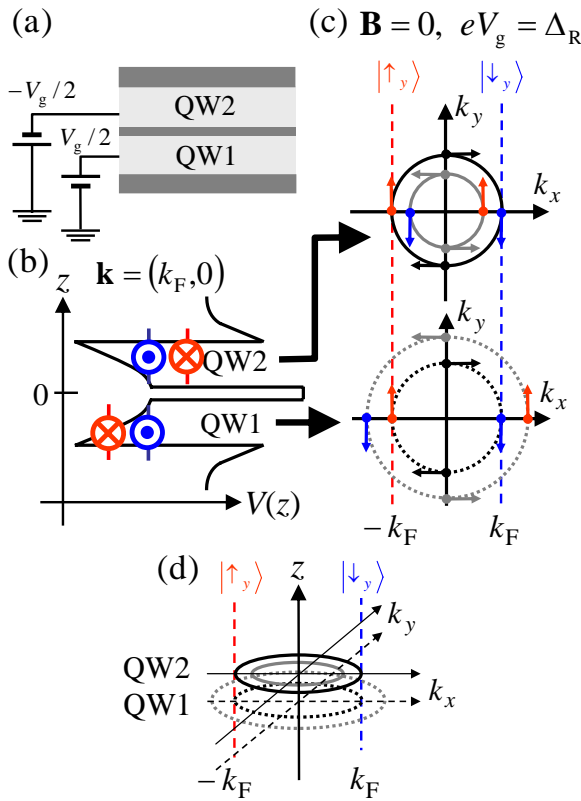


FIG. 6: (Color online) (a) Equivalent circuit model for the gated DQW without the applied magnetic field. (b) Spin-dependent eigenenergies in the DQW with $\mathbf{k} = (k_F, 0)$ and $V_g = \Delta_R/e$ [see (a) for V_g]. (c) Spin-dependent Fermi circle for independent QW1 and QW2 with $\mathbf{B} = 0$ and $V_g = \Delta_R/e$. (d) 3D illustration of the overlapped Fermi circles of the DQW with the given condition.

D. Failure of the spin-orbit blockade by the Fermi circle matching with gate

One may think that the same spin-blocking mechanism should be equally effective even if the size of the spin-dependent Fermi circles are controlled by the surface or back gate voltages, not by the in-plane magnetic field, but it is not the case as follows. Two Fermi circles of a selected spin can be made overlapped if the potential energies of QW1 and QW2 are shifted by a half of the Rashba splitting, i.e., $-\Delta_R/2$ and $\Delta_R/2$, respectively, or vice versa [see Fig. 2(b) for Δ_R]. We note that the change in the value of α_R by this gating is almost negligible in the InGaAs/InAlAs DQW because the gate voltage required to shift the potential energies by $\pm\Delta_R/2$ is very small. It turned out, however, that the proposed spin-blockade mechanism can not be validated by gating at least within the scheme of the simple one-dimensional model presented here.^{30,31}

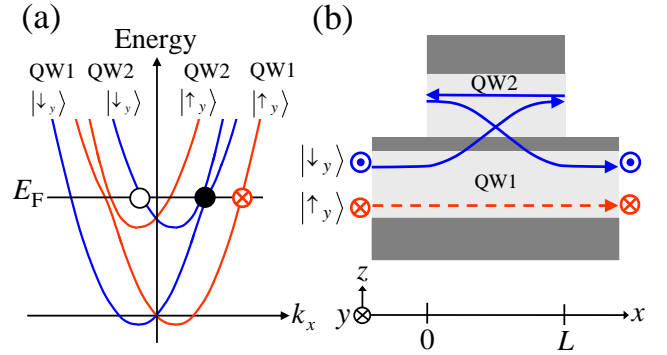


FIG. 7: (Color online) (a) Energy dispersion relation of the gated DQW with $V_g = \Delta_R/e$ [see Fig. 6(a) for V_g]. (b) Spin-dependent trajectories of an electrons which are injected in QW1 from left, where the Fermi wave number matching condition is satisfied by gate ($V_g = \Delta_R/e$).

For example, with $-\Delta_R/2$ and $\Delta_R/2$ for the shift of the potential energies in QW1 and QW2, respectively, and with $L = L_n$, the injected wave function $e^{ik_F x} |\Phi_{QW1}^{\downarrow y}\rangle$ at $x = 0$ connects to $|\Psi_{\text{inj}}^{\downarrow y}(x)\rangle$, which experiences a precessional motion between QW1 and QW2 as in the case of the application of the in-plane magnetic field B_{ac} [the point indicated with \bullet in Fig. 7(a)]. However, the wave function $|\Psi_{\text{inj}}^{\downarrow y}(x)\rangle$ at $x = L$ now connects to $e^{-i(k_F - 2k_\alpha)(x-L)} |\Phi_{QW2}^{\downarrow y}\rangle$ after backscattering in QW2 [\circ in Fig. 7(a)], which propagates back to $x = 0$ through QW2, where it gets reflected again. Then, this wave function again experiences a precessional motion from QW2 to QW1 and reach $x = L$ in QW1, where the electron is ejected to the right lead [curves marked with \odot in Fig. 7(b)]. On the other hand, for a spin-up electron injected at $x = 0$, $e^{i(k_F + 2k_\alpha)x} |\Phi_{QW1}^{\uparrow y}\rangle$ simply propagates through QW1 all the way to the right lead [broken line in Fig. 7(b)]. Therefore, both $e^{ik_F x} |\Phi_{QW1}^{\downarrow y}\rangle$ and $e^{i(k_F + 2k_\alpha)x} |\Phi_{QW1}^{\uparrow y}\rangle$ injected from the left lead of the device are eventually ejected to the right lead. This illustrates the failing mechanism of the spin-orbit blockade effect by gating instead of applying the in-plane magnetic field within the current simple one-dimensional model.³¹

III. TIGHT-BINDING MODEL DESCRIPTION OF THE PROPOSED DEVICE

A. Tight-binding model

Keeping in mind that the proposed spin-filtering device has the translational symmetry along the y -direction and

the front edge of the Fermi circle in \hat{k}_x carries the most of the electric current, we model the device by a tight-binding (TB) Hamiltonian³² consisting of a coupled one-dimensional chain as shown in Fig. 1(c),

$$\hat{H}_{k_y} = \sum_{\mathbf{m}, \sigma, \sigma'} \epsilon_{\mathbf{m} k_y}^{\sigma \sigma'} \hat{c}_{\mathbf{m} \sigma}^\dagger \hat{c}_{\mathbf{m} \sigma'} + \sum_{\mathbf{m}, \mathbf{m}', \sigma, \sigma'} \hat{c}_{\mathbf{m} \sigma}^\dagger t_{\mathbf{m} \mathbf{m}'}^{\sigma \sigma'} \hat{c}_{\mathbf{m}' \sigma'}, \quad (6)$$

where

$$\epsilon_{\mathbf{m} k_y}^{\sigma \sigma'} = \left[\frac{\hbar^2 k_y^2}{2m_{||}^*} + 2t_O \right] \delta_{\sigma \sigma'} + 2at_{\text{SO}}(m_z) k_y [\sigma_x]_{\sigma \sigma'} \quad (7)$$

and

$$t_{\mathbf{m} \mathbf{m}'}^{\sigma \sigma'} = \begin{cases} \left[-t_O \delta_{\sigma \sigma'} \mp it_{\text{SO}}(m_z) [\sigma_y]_{\sigma \sigma'} \right] \\ \times \exp(\mp i\phi(m_z)) & (\mathbf{m} = \mathbf{m}' \pm \mathbf{e}_x) \\ -t_{\text{coup}} \delta_{\sigma \sigma'} & (\mathbf{m} = \mathbf{m}' \pm \mathbf{e}_z) \\ 0 & (\text{otherwise}). \end{cases} \quad (8)$$

Here, $\hat{c}_{\mathbf{m} \sigma}$ ($\hat{c}_{\mathbf{m} \sigma}^\dagger$) is the annihilation (creation) operator of an electron at site $\mathbf{m} = (m_x, m_z)$ with spin σ ($=\uparrow, \downarrow$), where spin basis can be chosen in an arbitrary direction and m_x and m_z are the lattice site indices along the transport and out-of-plane directions, respectively. For m_z (=1 or 2), 1 and 2 represent QW1 and QW2, respectively. $t_O \equiv \hbar^2/2m_{||}^* a^2$ is the orbital hopping parameter where a is the lattice spacing along the transport direction ($a = 1$ nm in the present work). $t_{\text{SO}}(m_z) = (m_z - \frac{3}{2}) \alpha_R/a$ is the Rashba SOI hopping parameter along the x -direction within the m_z th QW. The tunneling between QW1 and QW2 is characterized by the inter-well coupling parameter t_{coup} , which is a half of the subband splitting for the unperturbed Hamiltonian H_0 in the absence of B [see Eq. (1) and Fig. 2(a)]. The effect of the applied magnetic field is incorporated as a form of Peierls phase factor

$$\phi(m_z) = 2\pi \frac{\Phi}{\Phi_0} \left(m_z - \frac{3}{2} \right), \quad (9)$$

where $\Phi_0 = h/e$ and $\Phi = 2Ba \langle z \rangle$ are the magnetic flux quantum and the magnetic flux threading through the TB unit cell, respectively. The left and right leads are also described by the TB Hamiltonian Eq. (6) but the lattice site along the out-of-plane direction is restricted to $m_z = 1$ (QW1), and the SOI coupling and magnetic field are set to zero. While our TB Hamiltonian [Eq. (6)] together with Eq. (10) below allows us to investigate on deterioration of the spin coherence by finite k_y component in the wave vector as following, our investigations in this article are restricted to the case with $k_y = 0$ to illustrate our fundamental idea of spin-blocking. First, the condition of spin-blocking for $k_y = 0$ (e.g., $B = B_{\text{ac}}$ in Fig. 10) is different from that for $k_y \neq 0$ and $k_x = \pm \sqrt{k_F^2 - k_y^2}$. Second, the first term in H_R in Eq. (1) [or the second term in Eq. (7)] results in the precession of up- and down-spins in the y direction. The detailed evaluation of such anti-spin-blocking effects is being in progress. It should

be possible to design an efficient device whose width W is smaller than its length L to reduce the anti-spin-blocking effects while W is large enough to carry a large current.

Once the Hamiltonian [Eq. (6)] is set, the spin-dependent electric current in the right lead is given as $I_{\uparrow, \downarrow} = G_{\uparrow, \downarrow} V_{\text{SD}}$ in the linear response regime, where V_{SD} is the spin-independent source-drain bias voltage. The zero-bias spin-dependent conductance $G_{\uparrow, \downarrow}$ associated with the right lead is expressed as follows in the Landauer-Büttiker formalism.³³

$$G_\sigma = \frac{e^2}{h} \sum_{k_y} \sum_{\sigma'=\uparrow, \downarrow} \int dE T_{\sigma \sigma', k_y}(E) \left\{ -\frac{df(E - E_F)}{dE} \right\}, \quad (10)$$

where $T_{\sigma \sigma', k_y}(E)$ is a transmission probability of an electron from the spin state σ' ($\sigma' = \uparrow, \downarrow$) in the left lead to the spin state σ ($\sigma = \uparrow, \downarrow$) in the right lead, assuming the conservation of k_y during transmission. In our simple model as mentioned above, we set $k_y = 0$ and skip the summation over k_y . Then, $T_{\uparrow, \downarrow, 0}(E) = T_{\downarrow, \uparrow, 0}(E) = 0$ if we choose the spin basis in \hat{y} , because \hat{H}_{k_y} commutes with σ_y . Thus, the spin-up and spin-down transmissions are treated separately. The spin-polarization of the electric current in the right lead is given by

$$P = \frac{I_\uparrow - I_\downarrow}{I_\uparrow + I_\downarrow} = \frac{G_\uparrow - G_\downarrow}{G_\uparrow + G_\downarrow}. \quad (11)$$

The actual numerical values of $T_{\sigma \sigma', k_y}$ can be calculated using the Recursive Green Function technique from the TB Hamiltonian [Eq. (6)] as elaborated in Ref. 32.

B. Values of the tight-binding parameters and the confirmation of the band dispersion of DQW

The actual material system of our choice to make the proposed device is $\text{In}_{0.53}\text{Ga}_{0.47}\text{As}/\text{In}_{0.52}\text{Al}_{0.48}\text{As}$ DQW,³⁴ where the well width d_{QW} for both QW1 and QW2 is 10 nm and the barrier thickness d_B ranges 1.5 – 5.0 nm. The donor doping (Si^+) in the carrier supplying layers above and below the DQW results in the electric fields along z axis within the DQW as explained in Sec. II. Other material specific parameters such as the energy band gap and the conduction band offset are given elsewhere.¹²

The following values are used in our actual calculations. $t_O = \hbar^2/2m_{||}^* a^2 = 0.81$ eV from $m_{||}^* = 0.047m_e$ and $a = 1$ nm. $t_{\text{SO}} = \alpha_R/2a = 1.57$ meV, where $\alpha_R = \frac{a_{\text{SO}}|e|N_S^{\text{tot}}/2}{2\epsilon_S \epsilon_0} = 3.14 \times 10^{-12}$ eVm assuming $\partial V(z)/\partial z = 0$ at the center of the barrier layer between QW1 and QW2 ($z = 0$). We note a_{SO} (intrinsic constant for the Rashba effect) = 25.28 Å² and ϵ_S (dielectric constant) = 13.1 for $\text{In}_{0.53}\text{Ga}_{0.47}\text{As}$ ³⁵. The total sheet carrier density N_S^{tot} was assumed to be 3.6×10^{16} m⁻² throughout the article. The values of t_{coup} (a half of the subband splitting) and $\langle z \rangle \equiv \langle \Phi_{\text{QW}2} | z | \Phi_{\text{QW}2} \rangle$ are obtained from the self-consistent solutions of the

one-band Poisson-Schrödinger equations of the unperturbed Hamiltonian H_0 with $B = 0$ [Eq. (1)] assuming the Neumann's boundary condition $\partial V(z)/\partial z = 0$ at $z = \pm(d_B/2 + 22)$ nm, which are just outside the 6 nm thick, symmetrically placed carrier supplying layers above and below the DQW, where the donor density is $1.8 \times 10^{16} \text{ m}^{-2}$ (a half of N_S^{tot}). It turned out that the values of t_{coup} and $\langle z \rangle$ approximately obey the following phenomenological equations: $t_{\text{coup}}(\text{eV}) = 11.66 e^{-1.09 d_B}$ and $\langle z \rangle(\text{nm}) = -1.105 e^{-1.12 d_B} + 5.744 + d_B/2$, where the unit for d_B is nm.

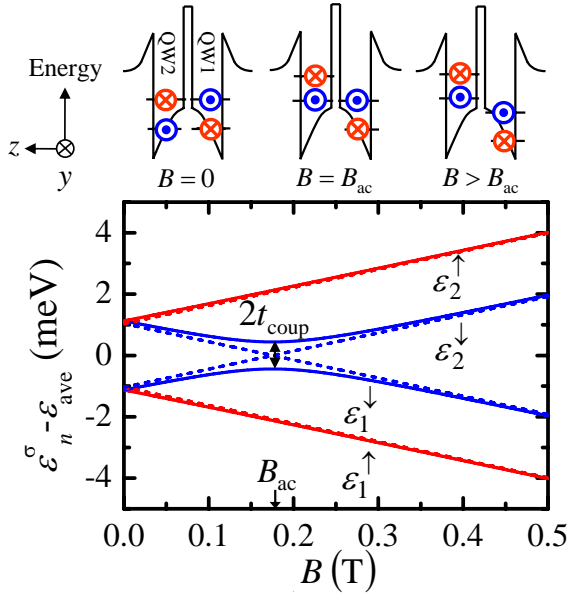


FIG. 8: (Color online) Energy eigenvalues in the symmetric DQW with $d_B = 3$ nm for a given wave vector $\mathbf{k} = (k_F, 0)$ ($k_F = 3.36 \times 10^8 \text{ m}^{-1}$) as a function of the in-plane magnetic field, where the solid and dashed curves correspond to the calculations with and without the inter-well coupling t_{coup} , respectively. ϵ_{ave} stands for the averaged energy $\epsilon_{\text{ave}} \equiv (\epsilon_1^{\uparrow} + \epsilon_1^{\downarrow} + \epsilon_2^{\uparrow} + \epsilon_2^{\downarrow})/4$. On top of the main figure, we depict the spin-dependent energy levels for $t_{\text{coup}} = 0$ at three representative magnetic fields.

The correspondence between the continuous effective mass model [Eq. (1)] and the TB model [Eq. (6)] is made clear if one diagonalizes the following 4×4 TB Hamiltonian of the DQW part of the device in the spin \otimes QW space for a unit cell, taking into account the k_x -dependent Bloch phase assuming the translational symmetry along the x direction, which is equivalent to applying the periodic boundary condition.

$$H^{\text{spin}\otimes\text{QW}} \equiv e^{-ik_x a} H_{0,-1} + H_{0,0} + e^{ik_x a} H_{0,+1}, \quad (12)$$

where

$$H_{0,0} = \begin{pmatrix} 2t_O & 0 & -t_{\text{coup}} & 0 \\ 0 & 2t_O & 0 & -t_{\text{coup}} \\ -t_{\text{coup}} & 0 & 2t_O & 0 \\ 0 & -t_{\text{coup}} & 0 & 2t_O \end{pmatrix} \quad (13)$$

and

$$H_{0,\pm 1} = \begin{pmatrix} \langle m_x | \langle m_x | \langle m_x | \langle m_x | \\ 1 \uparrow & 1 \downarrow & 2 \uparrow & 2 \downarrow \\ t_{\text{QW}1}^{\uparrow\uparrow} & t_{\text{QW}1}^{\uparrow\downarrow} & 0 & 0 \\ t_{\text{QW}1}^{\downarrow\uparrow} & t_{\text{QW}1}^{\downarrow\downarrow} & 0 & 0 \\ 0 & 0 & t_{\text{QW}2}^{\uparrow\uparrow} & t_{\text{QW}2}^{\uparrow\downarrow} \\ 0 & 0 & t_{\text{QW}2}^{\downarrow\uparrow} & t_{\text{QW}2}^{\downarrow\downarrow} \end{pmatrix} \begin{array}{l} |m_x \pm 1, m_z = 1, \uparrow \rangle \\ |m_x \pm 1, m_z = 1, \downarrow \rangle \\ |m_x \pm 1, m_z = 2, \uparrow \rangle \\ |m_x \pm 1, m_z = 2, \downarrow \rangle \end{array} \quad (14)$$

are the couplings among the 4 sites in the spin \otimes QW space at the m_x th lattice site and those between the m_x th and $(m_x \pm 1)$ th lattice sites, respectively. In Eq. (14), the matrix elements $t_{\text{QW}1}^{\sigma\sigma'}$ and $t_{\text{QW}2}^{\sigma\sigma'}$ are given by $t_{\mathbf{m},\mathbf{m}\pm\mathbf{e}_x}^{\sigma\sigma'}$ of Eq. (8) with $m_z = 1$ and 2 for QW1 and QW2, respectively.

Choosing the spin basis in \hat{y} , $H^{\text{spin}\otimes\text{QW}}$ can be block diagonalized and solved separately for each spin. The sorted spin-up and -down Hamiltonians are

$$H_{\uparrow,\downarrow} = 2t_O I_{\text{QW}} - 2\sqrt{t_O^2 + t_{\text{SO}}^2} \times \begin{pmatrix} \cos(k_x a + \tilde{\phi}_{\uparrow,\downarrow}) & \tilde{t}_{\text{coup}} \\ \tilde{t}_{\text{coup}} & \cos(k_x a - \tilde{\phi}_{\uparrow,\downarrow}) \end{pmatrix} \quad (15)$$

in the QW space. We note $\tilde{t}_{\text{coup}} = t_{\text{coup}}/2\sqrt{t_O^2 + t_{\text{SO}}^2}$ and $\tilde{\phi}_{\uparrow,\downarrow} = \phi \pm \tilde{\alpha}$ (+ for \uparrow and $-$ for \downarrow), where $\phi = eBa \langle z \rangle/\hbar$ and $\tilde{\alpha} = \tan^{-1}(t_{\text{SO}}/t_O)$. I_{QW} is the 2×2 identity matrix in the QW space. The eigenvalues of this Hamiltonian, which provide the spin-dependent energy dispersion relations for the DQW system in the presence of the Rashba SOI and in-plane magnetic field, are

$$\epsilon_{1,2}^{\uparrow\downarrow} = 2t_O - 2\sqrt{t_O^2 + t_{\text{SO}}^2} \cos k_x a \cos \tilde{\phi}_{\uparrow,\downarrow} \pm \sqrt{t_{\text{coup}}^2 + 4(t_O^2 + t_{\text{SO}}^2) \left(\sin k_x a \sin \tilde{\phi}_{\uparrow,\downarrow} \right)^2}, \quad (16)$$

where $-$ and $+$ signs are for subbands 1 and 2, respectively. One finds that these energies agree with the results of the effective mass model in Eq. (1) within 1% at the Fermi energy by Taylor expanding the trigonometric functions in Eq. (16), where the following values are sufficiently smaller than unity: $k_x a \approx k_F a = 0.336$, $\phi \approx 4.3 \times 10^{-3}$ (for $B = 0.2$ T and $\langle z \rangle = 7$ nm) and $\tilde{\alpha} \approx t_{\text{SO}}/t_O = 1.9 \times 10^{-3}$.

In Fig. 8, we plot the magnetic field dependence of these eigenenergies for $d_B = 3$ nm ($t_{\text{coup}} = 0.44$ meV) and $k_x = k_F = 3.36 \times 10^8 \text{ m}^{-1}$ relative to their averaged value, together with the results when the coupling between QW1 and QW2 is turned off ($t_{\text{coup}} = 0$). Here energy difference between the spin degenerate pairs $\epsilon_2^{\uparrow,\downarrow}$ and $\epsilon_1^{\uparrow,\downarrow}$

at $B = 0$, which is interpreted as the subband splitting in the symmetric DQW, is very close in value to the Rashba splitting energy $2\alpha_R k_F$ of independent QW1 and QW2. This is because the orbital parts of the eigenfunctions for each spin-degenerate subband level are localized in either QWs depending on their spin state [Fig. 2(a)]. The slopes for $B \rightarrow 0$ T in Fig. 8 with $t_{\text{coup}} = 0$ are given exactly by $\pm\hbar e \langle z \rangle k_F / m_{||}^* = \pm 5.97$ meV/T. Upon increasing B , Fig. 8 shows that the energy levels ε_1^\downarrow and ε_2^\downarrow anticross each other at $B = B_{\text{ac}} \equiv m_{||}^* \alpha_R / \hbar \langle z \rangle = 0.177$ T, where $\tilde{\phi}_\downarrow = \phi - \tilde{\alpha} = 0$ and Eq. (16) reduces to $\varepsilon_{1,2}^\downarrow = 2t_O - 2\sqrt{t_O^2 + t_{\text{SO}}^2} \cos k_x a \pm t_{\text{coup}}$. This means that the anticrossing energy gap found in Fig. 8 is exactly the subband splitting energy in the absence of both the Rashba SOI and the magnetic field [Fig. 2(a)]. Thus the bonding and antibonding states are formed selectively for spin-down electrons. Spin-up wavefunctions are then localized in either QW1 or QW2. As we further increase the magnetic field ($B > B_{\text{ac}}$), both the spin-up and -down wave functions are localized in either QW1 or QW2 (see the top pictures in Fig. 8).

IV. TRANSPORT ANALYSIS AND SPIN FILTERING PROPERTIES

In Fig. 9, we plotted the calculated values of the spin-dependent conductances $G_{\uparrow,\downarrow}$ ($\uparrow \parallel \hat{y}$) as a function of L at $B = B_{\text{ac}}$ for $d_B = 2$ and 3 nm ($T = 5$ K). We find that the change in the value of G_\downarrow as a function of L is more pronounced than that of G_\uparrow , where G_\downarrow even becomes zero at specific device lengths L_n^* , n being an integer, while G_\uparrow varies only weakly with L . These qualitative behaviors are in agreement with the argument in Sec. II. We find that $L_1^* = 648$ nm and $L_2^* = 1946$ nm for $d_B = 2$ nm, whereas $L_1 = 646$ nm and $L_2 = 1939$ nm in Sec. III. Similarly, $L_1^* = 1914$ nm here agrees with $L_1 = 1906$ nm in Sec. II for $d_B = 3$ nm. We note $L_n \equiv \pi(n - \frac{1}{2}) / k_{\text{coup}}$, where $k_{\text{coup}} = t_{\text{coup}}(dE(k)/dk)^{-1} \approx t_{\text{coup}} m_{||}^* a / \hbar^2 \sin(k_F a)$ in the TB model.

Shown in Fig. 10 are the magnetic field dependence of $G_{\uparrow,\downarrow}$ for $d_B = 2$ nm and 3 nm, where the values of L are 646 and 1906 nm, respectively. For $B > 0$, we observe that G_\downarrow becomes zero at $B = 0.192$ T and 0.177 T for $d_B = 2$ nm and 3 nm, respectively, i.e., at the anticrossing magnetic field B_{ac} . For $B < 0$, on the other hand, G_\uparrow reaches zero at $B = -B_{\text{ac}}$ while G_\downarrow is kept close to unity, as is consistent with the symmetry found in the Hamiltonian [Eq. (1)]. In Fig. 10, we also recognize that the variation of G_\downarrow (G_\uparrow) around $B = B_{\text{ac}}$ ($B = -B_{\text{ac}}$) is more moderate for $d_B = 2$ nm than for $d_B = 3$ nm. This is because the bonding/antibonding states $(1/\sqrt{2} \{|\Psi_b\rangle \pm |\Psi_a\rangle\})$ at $B = \pm B_{\text{ac}}$ are more robust with the change of B for $d_B = 2$ nm than for $d_B = 3$ nm because of the stronger inter-well coupling t_{coup} . The range of the magnetic field ΔB around $B = B_{\text{ac}}$

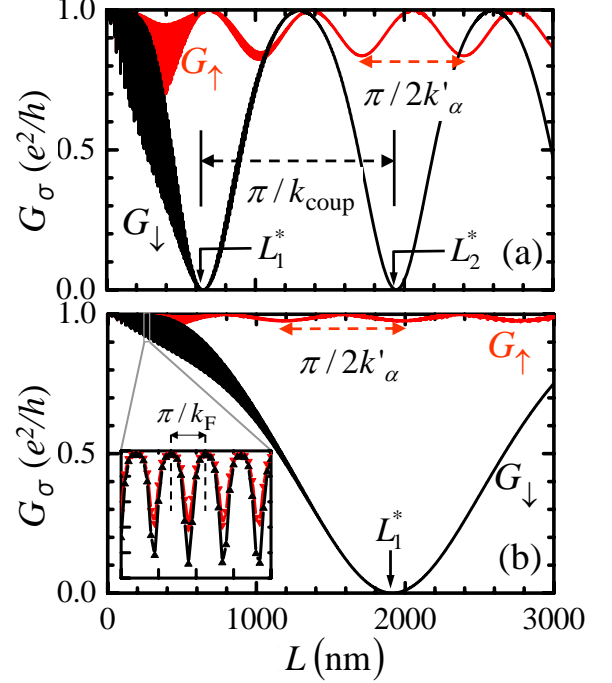


FIG. 9: (Color online) Plots of the spin-dependent conductances $G_{\uparrow,\downarrow}$, calculated for two different barrier thicknesses (a) $d_B = 2$ nm and (b) $d_B = 3$ nm as a function of the device length L . The magnetic fields are fixed at their anticrossing values $B_{\text{ac}} = 0.192$ T for (a) and 0.177 T for (b). The inset of (b) is the magnified view of the main panel between 260 nm and 300 nm for abscissa and between $0.9 e^2/h$ and $1.0 e^2/h$ for ordinate, where the period of the rapid oscillations is found to be π/k_F .

within which the bonding/antibonding states persist can be roughly estimated by equating $e\Delta B \langle z \rangle / \hbar$ to k_{coup} . We obtain $\Delta B = 0.24$ T and 0.075 T for $d_B = 2$ nm and $d_B = 3$ nm, respectively, which agree well with the widths of conductance dips observed in Fig. 10. Thus, measuring the width of the magneto-conductance dip would provide an estimate of the value of t_{coup} .

We note that there are features in Fig. 9 that cannot be explained by the simple flying qubit model (Sec. II). The first is the rapid oscillation of the spin-dependent conductance as shown in the inset of Fig. 9(b). We notice that these oscillations (i) are more pronounced for shorter L , (ii) disappear as $G_{\uparrow,\downarrow}$ approaches to zero or the maximum value e^2/h , and (iii) damp away with increasing L . The period of the rapid oscillation, which is essentially constant with L , is found to be $\Delta L \simeq 9.34$ nm.³⁶ This is in good agreement with the value of π/k_F , which infers some resonance phenomena associated with the plane wave part of the electron wave function. Detailed analysis using the multiple reflection model (Appendix B) revealed that it is not the discontinuities in

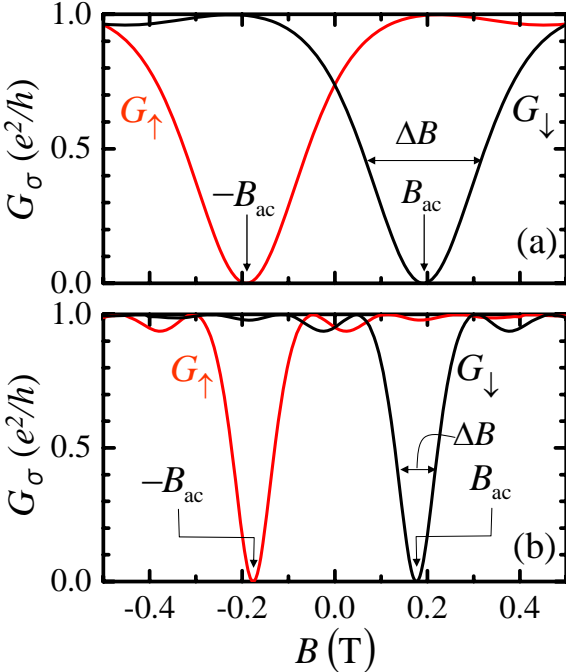


FIG. 10: (Color online) Magnetic field dependence of the spin-dependent conductances for (a) $d_B = 2$ nm and (b) $d_B = 3$ nm. The device lengths for $d_B = 2$ nm and 3 nm are $L = 646$ nm and 1906 nm, respectively. The anti-crossing magnetic fields B_{ac} for $d_B = 2$ nm and 3 nm are 0.192 T and 0.177 T, respectively, as indicated in the figures. See text for the explanation of ΔB .

the values of B and/or α_R in the Hamiltonian between the leads and the DQW but the finite probability amplitude of the electron wave function within QW2 which resulted from tunneling from QW1, that caused the wave function reflection at $x = 0$ and L . The reason for the disappearance of the rapid oscillations as G_\downarrow approaches to zero or e^2/h is the disappearance of the wave function amplitude within QW2 at either $x = 0$ or L with the condition $L = L_n^*$ or $L = L_n^* + \pi/2k_{\text{coup}}$, respectively.³⁷

Second, the damping of the rapid oscillations with increasing L in Fig. 9 is due to the finite temperature assumed in our calculation. Considering the finite width Δk in the wave number values that participates in the electron transport, the criteria for having this rapid oscillation is $\Delta kL \ll 1$. Using $\Delta k = k_B T (\partial E / \partial k)^{-1} \approx 8 \times 10^{-5} \text{ m}^{-1}$ for $T = 5$ K, we obtain $L \ll 1.25 \mu\text{m}$, which explains the decay of the rapid oscillation with increasing L .

Another feature in Fig. 9 that cannot be explained by the simple flying qubit model in Sec. II is the weak modulation of the spin-up conductance G_\uparrow with period $\pi/2k'_\alpha$ in Fig. 9, where k'_α is the corrected Rashba wave

number (see below). This modulation of G_\uparrow can be explained qualitatively by the following extended qubit model (see Appendix B for the exact model). It turned out that even the eigenfunctions of the spin-up electrons are more correctly described as superpositioned states between QW1 and QW2 because the inter-well coupling t_{coup} is not completely negligible for the spin-up electrons either. These eigenfunctions still keep the features of antibonding-like or bonding-like wave functions in a sense whether they have a node or not, respectively,

$$|\Phi_a^\uparrow\rangle = \delta |\Phi_{\text{QW}1}^\uparrow\rangle - \sqrt{1-\delta^2} |\Phi_{\text{QW}2}^\uparrow\rangle, \quad (17)$$

$$|\Phi_b^\uparrow\rangle = \sqrt{1-\delta^2} |\Phi_{\text{QW}1}^\uparrow\rangle + \delta |\Phi_{\text{QW}2}^\uparrow\rangle, \quad (18)$$

where $0 < \delta < 1$, apart from the plane wave part for the in-plane transport. We obtained $\delta = 0.275$ and 0.104 for $d_B = 2$ nm and 3 nm, respectively, from the eigenvectors of the spin-up Hamiltonian [Eq. (12)]. For electrons propagating in the positive x direction, the in-plane wave numbers for $|\Phi_b^\uparrow\rangle$ and $|\Phi_a^\uparrow\rangle$ are $k_F + 2k'_\alpha$ and $k_F - 2k'_\alpha$, respectively, where the corrected Rashba wave number k'_α is $k_\alpha + k_{\text{coup}}^2/8k_\alpha$ incorporating the contribution of the inter-well coupling t_{coup} to the wave number shift (see Appendix A). After similar procedures as in Sec. II, which we call as the extended flying qubit model, we obtain the following expression for the transmission probability of the spin-up electrons,

$$T_{\uparrow(\text{QW}1)} = 1 - 4\delta^2(1-\delta^2) \sin^2(2k'_\alpha L). \quad (19)$$

Thus, the periods of conductance modulation for spin-up electron are $\pi/2k'_\alpha = 677$ nm and 792 nm for $d_B = 2$ nm and 3 nm, respectively, which are in good agreement with 683 nm and 799 nm in the TB calculation (Fig. 9). We note that the extended flying qubit model overestimates the oscillation amplitudes of G_\uparrow , i.e., $4\delta^2(1-\delta^2) = 0.2805$ and 0.0429 in units of e^2/h for $d_B = 2$ nm and 3 nm, respectively, whereas the corresponding values in the TB calculations are about half of these. The discrepancy comes from the absence of both the multiple reflections of wave function between $x = 0$ and L and the thermal averaging effect in our naive model. We derived the exact results assuming multiple reflections between $x = 0$ and L which reproduced the TB results in Appendix B.

V. CONCLUSION

We proposed a lateral spin-blockade device using InGaAs/InAlAs double quantum well (DQW), where the values of the Rashba spin-orbit parameter α_R are opposite in sign but equal in magnitude between the constituent quantum wells (QW). The principle of the spin-blocking effect in the proposed device is in the spin-selective matching of the front and back edges of the spin-split Fermi circles [Fermi circle points at $(\pm k_F, 0)$] between the two QWs, which is made possible by the

in-plane magnetic field $\mathbf{B} = (0, B_{\text{ac}}, 0)$. The superposition of the resulting bonding and antibonding wavefunctions that are formed for the selected (e.g., spin-down) electrons exclusively results in the precessional motion of electrons between the QW1 and QW2, which is denoted as the “flying qubit” state. The “flying qubit” state can be blocked by depleting or etching away only the QW2 part at a length of half-integer multiple of the precession wave length as depicted in Fig. 5(b).

We would like to reiterate the features of the proposed spin-filtering device. (i) The proposed device is novel in a sense that it operates based on the conventional band theory and the Boltzmann transport theory, adding the spin degree of freedom in the form of the Rashba effect. Thus, only the elementary level of quantum mechanics and solid state physics is required to understand the principle of the device. (ii) In our simplified one-dimensional model where two singly-channeled leads are attached to the device, we obtain a perfect spin-blockade by the in-plane magnetic field $\mathbf{B} = (0, B_{\text{ac}}, 0)$, whereas such spin-blocking fails to happen in the case of electrical control using the gate. The latter observation is found to be consistent with the recent theoretical results proven analytically for devices with two singly-channeled leads. (iii) The actual devices, however, will be prepared in the form of the two-dimensional electron gas (2DEG), where finite k_y components ($\perp \mathbf{I}$) in the electron wave vector also participate in the electron transport. While some deterioration in the spin-polarization will be expected in the actual 2D model due to the finite k_y components, the multi-channeled nature of the device would, in turn, allow the generation of spin-polarized current purely electrically. We can expect that the spin-polarized currents thus generated are fairly large due to the multi-channeled nature of the device, as compared to those generated by the QPC-based devices, for example, which open the possibilities of future spintronics applications widely.

Acknowledgment

This work was supported by KAKENHI, Grant-in-Aid for Scientific Research (B), Grant No. 23360001.

Appendix A : Correction to the Rashba wave number k_α due to the inter-well coupling t_{coup}

The generalized Rashba wave number k'_α is associated with the energy difference $\varepsilon_2^\uparrow - \varepsilon_1^\uparrow$ with $\mathbf{B} = (0, B_{\text{ac}}, 0)$ at the Fermi wave number as following [see Eq. (16)].

$$\begin{aligned} \varepsilon_2^\uparrow - \varepsilon_1^\uparrow &= 2\sqrt{t_{\text{coup}}^2 + 4(t_0^2 + t_{\text{SO}}^2) \left(\sin k_F a \sin \tilde{\phi}_\downarrow \right)^2} \\ &\equiv 4k'_\alpha \left. \frac{\partial E(k_x)}{\partial k_x} \right|_{k_x=k_F} \end{aligned} \quad (20)$$

In the limit $a \rightarrow 0$, we have $\tilde{\phi}_\downarrow = \phi + \tan^{-1}(t_{\text{SO}}/t_0) = 2t_{\text{SO}}/t_0$, where $\phi = eB_{\text{ac}}a \langle z \rangle / \hbar = t_{\text{SO}}/t_0$, $t_{\text{SO}}/t_0 = k_\alpha a$, and $t_{\text{coup}} = \hbar^2 k_F k_{\text{coup}} / m_{||}^*$. Note $t_0 = \hbar^2 / 2m_{||}^* a^2$. Substituting these in Eq. (20) and letting $a \rightarrow 0$, we have

$$\begin{aligned} \varepsilon_2^\uparrow - \varepsilon_1^\uparrow &= \frac{4\hbar^2 k_F x k_\alpha}{m_{||}^*} \sqrt{1 + \frac{k_{\text{coup}}^2}{4k_\alpha^2}} \\ &\approx 4k_\alpha \left(1 + \frac{k_{\text{coup}}^2}{8k_\alpha^2} \right) \left. \frac{\partial E(k_x)}{\partial k_x} \right|_{k_x=k_F}, \end{aligned} \quad (21)$$

for $k_{\text{coup}} < k_\alpha$. Comparing Eqs. (20) and (21), we obtain

$$k'_\alpha \approx k_\alpha + \frac{k_{\text{coup}}^2}{8k_\alpha}. \quad (22)$$

Appendix B: Multiple reflection model

Consider a DQW device with length L . Let $t_{mm'}$ ($m, m' = 1, 2$) be the nominal quantum mechanical transmission amplitude of electron from $x = 0$ in QW m' to $x = L$ in QW m . Similarly we let $r_{mm'}$ be the nominal transmission amplitude of electron from $x = L$ in QW m' to $x = 0$ in QW m . The multiple reflection model states that the overall transmission amplitude from QW1 at $x = 0$ to QW1 at $x = L$ is given by

$$\begin{aligned} t_{\text{tot}} &= t_{11} + t_{12}r_{22}t_{21} + t_{12}r_{22}t_{22}r_{22}t_{21} + \dots \\ &= t_{11} + t_{12}r_{22} \left\{ 1 + (t_{22}r_{22}) + (t_{22}r_{22})^2 + \dots \right\} t_{21} \\ &= t_{11} + \frac{t_{12}r_{22}t_{21}}{1 - t_{22}r_{22}}, \end{aligned} \quad (23)$$

where the transmission probability T_{tot} is given by $|t_{\text{tot}}|^2$. The values of $t_{mm'}$ and $r_{mm'}$ per spin are obtained by the generalized flying qubit model as following.

Choosing the spin quantization axis in \hat{y} , the eigenfunctions in DQW without spin are $e^{\pm i(k_F + \Delta k)x} |\Phi_b\rangle$ and $e^{\pm i(k_F - \Delta k)x} |\Phi_a\rangle$ at $E = E_F$ and $\mathbf{B} = (0, B_{\text{ac}}, 0)$, where

$$|\Phi_b\rangle = \sqrt{1 - \delta^2} |\Phi_{\text{QW}1}\rangle + \delta |\Phi_{\text{QW}2}\rangle, \quad (24)$$

$$|\Phi_a\rangle = \delta |\Phi_{\text{QW}1}\rangle - \sqrt{1 - \delta^2} |\Phi_{\text{QW}2}\rangle \quad (25)$$

($0 < \delta < 1$). We note $\Delta k = k_{\text{coup}}$ or $2k'_\alpha$ for spin-up or spin-down electrons, respectively, and ${}^t(\sqrt{1 - \delta^2}, \delta)$ and ${}^t(\delta, -\sqrt{1 - \delta^2})$ are the eigenvectors of Eq. (15). We solve these for $|\Phi_{\text{QW}1}\rangle$ and $|\Phi_{\text{QW}2}\rangle$.

$$|\Phi_{\text{QW}1}\rangle = \sqrt{1 - \delta^2} |\Phi_b\rangle + \delta |\Phi_a\rangle \quad (26)$$

$$|\Phi_{\text{QW}2}\rangle = \delta |\Phi_b\rangle - \sqrt{1 - \delta^2} |\Phi_a\rangle \quad (27)$$

We let these wave functions propagate from $x = 0$ to

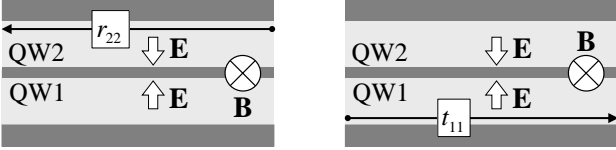


FIG. 11: Schematic illustration for symmetry consideration. The nominal transmission amplitude through QW2 with negative k_x (r_{22} in the left panel) is found to be equal to that through QW1 with positive k_x (t_{11} in the right panel).

$$x = L.$$

$$\begin{aligned}
 & |\Phi_{\text{QW1}}\rangle \text{ (at } x = 0) \\
 & \rightarrow e^{ik_F L} \left\{ e^{i\Delta k L} \sqrt{1 - \delta^2} |\Phi_b\rangle + e^{-i\Delta k L} \delta |\Phi_a\rangle \right\} \\
 & = e^{ik_F L} \left[\left\{ e^{i\Delta k L} - 2i\delta^2 \sin(\Delta k L) \right\} |\Phi_{\text{QW1}}\rangle \right. \\
 & \quad \left. + 2i\delta \sqrt{1 - \delta^2} \sin(\Delta k L) |\Phi_{\text{QW2}}\rangle \right] \\
 & \text{(at } x = L) \\
 \\
 & |\Phi_{\text{QW2}}\rangle \text{ (at } x = 0) \\
 & \rightarrow e^{ik_F L} \left\{ e^{i\Delta k L} \delta |\Phi_b\rangle + e^{-i\Delta k L} \sqrt{1 - \delta^2} |\Phi_a\rangle \right\} \\
 & = e^{ik_F L} \left[2i\delta \sqrt{1 - \delta^2} \sin(\Delta k L) |\Phi_{\text{QW1}}\rangle \right. \\
 & \quad \left. + \left\{ e^{-i\Delta k L} + 2i\delta^2 \sin(\Delta k L) \right\} |\Phi_{\text{QW2}}\rangle \right] \\
 & \text{(at } x = L) \tag{28}
 \end{aligned}$$

From these we obtain

$$t_{11} = e^{ik_F L} \left\{ e^{i\Delta k L} - 2i\delta^2 \sin(\Delta k L) \right\}, \tag{29}$$

$$t_{12} = e^{ik_F L} \left\{ 2i\delta \sqrt{1 - \delta^2} \sin(\Delta k L) \right\}, \tag{30}$$

$$t_{21} = e^{ik_F L} \left\{ 2i\delta \sqrt{1 - \delta^2} \sin(\Delta k L) \right\} \tag{31}$$

and

$$t_{22} = e^{ik_F L} \left\{ e^{-i\Delta k L} + 2i\delta^2 \sin(\Delta k L) \right\}. \tag{32}$$

Now we let $|\Phi_{\text{QW2}}\rangle$ propagate from $x = L$ to $x = 0$ to obtain r_{22} . After a simple symmetry consideration in Fig. 11, we notice that it is equal to t_{11} .

$$r_{22} = t_{11} = e^{ik_F L} \left\{ e^{i\Delta k L} - 2i\delta^2 \sin(\Delta k L) \right\}. \tag{33}$$

Substituting Eqs. (29)–(32) and (33) into Eq. (23), we have

$$t_{\text{tot}} = \frac{e^{ik_F L} (1 - e^{2ik_F L}) [e^{i\Delta k L} - i\delta^2 \sin(k_F L)]}{1 - e^{2ik_F L} T_{11}}, \tag{34}$$

where $T_{11} = |t_{11}|^2 = 1 - 4\delta^2(1 - \delta^2) \sin^2(\Delta k L)$ is the result of the extended qubit model. We obtain the overall transmission probability as

$$T_{\text{tot}} = |t_{\text{tot}}|^2 = \frac{2 [1 - \cos(2k_F L)] T_{11}}{1 - 2T_{11} \cos(2k_F L) + T_{11}^2}. \tag{35}$$

We confirmed that this reproduces the TB results quantitatively. We note that the spin-dependence of T_{tot} is realized only through T_{11} . Thermal average of T_{tot} is also straightforward.

¹ S. Datta and B. Das, *Appl. Phys. Lett.* **56**, 665 (1990).
² E. I. Rashba, *Fiz. Tverd. Tela (Leningrad)* **2**, 1224 (1960) [*Sov. Phys. Solid State* **2**, 1109 (1960)]; Y. A. Bychkov and E. I. Rashba, *J. Phys. C* **17**, 6039 (1984).
³ J. Nitta, T. Akazaki, H. Takayanagi and T. Enoki, *Phys. Rev. Lett.* **78**, 1335 (1997).
⁴ T. Koga, J. Nitta, T. Akazaki, and H. Takayanagi, *Phys. Rev. Lett.* **89**, 046801 (2002).
⁵ R. Fiederling, M. Keim, G. Reuscher, W. Ossau, G. Schmidt, A. Waag, and L. W. Molenkamp, *Nature* **402**, 787 (1999); Y. Ohno, D. K. Young, B. Beschoten, F. Matsukura, H. Ohno and D. D. Awschalom, *ibid.* **402**, 790 (1999).
⁶ A. T. Filip, P. LeClair, C. J. P. Smits, J. T. Kohlhepp, H. J. M. Swagten, B. Koopmans, and W. J. M. de Jonge, *Appl. Phys. Lett.* **81**, 1815 (2002).
⁷ J. E. Hirsch, *Phys. Rev. Lett.* **83**, 1834 (1999).
⁸ S. Murakami, N. Nagaosa, and S.-C.-Zhang, *Science* **301**, 1348 (2003).
⁹ Y. K. Kato, R. C. Myers, A. C. Gossard, D. D. Awschalom, *Science* **306**, 1910 (2004).
¹⁰ J. Wunderlich, B. Kaestner, J. Sinova, and T. Jungwirth, *Phys. Rev. Lett.* **94**, 047204 (2005).
¹¹ A. Voskoboynikov, S. S. Lin, C. P. Lee, and O. Tretyak, *J. Appl. Phys.* **87**, 387 (2000).
¹² T. Koga, J. Nitta, H. Takayanagi, and S. Datta, *Phys. Rev. Lett.* **88**, 126601-1 (2002); T. Koga, J. Nitta, T. Akazaki, and H. Takayanagi, *Jpn. J. Appl. Phys.* **41** 2501 (2002).
¹³ D. Z.-Y. Ting and X. Cartoixà, *Appl. Phys. Lett.* **81**, 4198 (2002).
¹⁴ M. Eto, T. Hayashi, and Y. Kurotani, *J. Phys. Soc. Jan.* **74** 1934 (2005).
¹⁵ P. Debray, S. M. S. Rahman, J. Wan, R. S. Newrock, M. Cahay, A. T. Ngo, S. E. Ulloa, S. T. Herbert, M. Muhammad, and M. Johnson, *Nature Nanotech.* **4**, 759 (2009).
¹⁶ M. Kohda, S. Nakamura, Y. Nishihara, K. Kobayashi, T. Ono, J. Ohe, Y. Tokura, T. Mineno, and J. Nitta, *Nature Commun.* **3**, 1082 (2012).
¹⁷ S. Kim, Y. Hashimoto, Y. Iye, and S. Katsumoto, *J. Phys. Soc. Jpn.* **81**, 054706 (2012).
¹⁸ C. L. Kane and E. J. Mele, *Phys. Rev. Lett.* **95**, 226801 (2005).
¹⁹ B. A. Bernevig, T. L. Hughes, and S. C. Zhang, *Science* **314**, 1757 (2006).
²⁰ K. Ando and E. Saitoh, *Nat. Commun.* **3**, 629 (2012).
²¹ T. Matsuura, S. Faniel, N. Monta, and T. Koga, *Physica E* **42**, 2707 (2010).

²² E. Bernardes, J. Schliemann, M. Lee, J. C. Egues, and D. Loss, Phys. Rev. Lett. **99**, 076603 (2007).

²³ M. M. Glazov, M. A. Semina, S. M. Badalyan, and G. Vignale, Phys. Rev. B **84**, 033305 (2011).

²⁴ U. Ekenberg and D. M. Gvozdić, Phys. Rev. B **78**, 205317 (2008).

²⁵ $\langle E_z \rangle_{1,2} \equiv \langle \Phi_{\text{QW}1,2} | E_z(z) | \Phi_{\text{QW}1,2} \rangle$, where $|\Phi_{\text{QW}1,2}\rangle \equiv 1/\sqrt{2}\{|\Psi_b\rangle \pm |\Psi_a\rangle\}$, letting $|\Psi_b\rangle$ and $|\Psi_a\rangle$ be the lowest (bonding-like) and the second lowest (antibonding-like) energy eigenstates of the unperturbed DQW Hamiltonian along z direction (normal to the QW plane) with $B = 0$ [see Eq. (1)]. The sign in $\{|\Psi_b\rangle \pm |\Psi_a\rangle\}$ should be chosen in such a way that $|\Phi_{\text{QW}1}\rangle$ and $|\Phi_{\text{QW}2}\rangle$ have values in QW1 and QW2, respectively.

²⁶ Assuming a plane wave for the in-plane part of the wave function, the operators $\frac{\partial}{i\partial x}$ and $\frac{\partial}{i\partial y}$ are replaced with the c -numbers k_x and k_y , respectively.

²⁷ Using typical values for InGaAs/InAlAs QWs ($g^* = -3$, $B = 0.2$ T, $\alpha_R = 3.1429 \times 10^{-12}$ eVm, $k_x = 3.3621 \times 10^8$ m $^{-1}$ and $z = 7$ nm), we obtain $\alpha_R k_x = 1.06$ meV, $\alpha_R e B z / \hbar = 6.68$ μ eV and $-g^* \mu_B B / 2 = 17.4$ μ eV. See J. Nitta, Y. Lin, T. Akazaki, and T. Koga, Appl. Phys. Lett. **83**, 4565 (2003); F. E. Meijer, A. F. Morpurgo, T. M. Klapwijk, T. Koga, and J. Nitta, Phys. Rev. B **70**, 201307(R) (2004); X. Z. Liu, Y. G. Xu, G. Yu, L. M. Wei, T. Lin, S. L. Guo, J. H. Chu, W. Z. Zhou, Y. G. Zhang, and D. J. Lockwood, J. Appl. Phys. **113**, 033704 (2013) for g^* values in InGaAs/InAlAs QWs.

²⁸ S. Faniel, T. Matsuura, S. Mineshige, Y. Sekine, and T. Koga, Phys. Rev. B **83**, 115309 (2011).

²⁹ C.-M. Hu and D. Heitmann, App. Phys. Lett. **77**, 1475 (2000).

³⁰ It turned out that the vanishment of spin-polarization in any SOI-controled device with two singly-channeled leads attached is mathematically proven; see J. J. Krich and B. I. Halperin, Phys. Rev. B **78** 035338 (2008), F. Zhai and H. Q. Xu, Phys. Rev. Lett. **94**, 246601 (2005), A. A. Kiselev and K. W. Kim, Phys. Rev. B **71**, 153315 (2005), and A. A. Kiselev and K. W. Kim, J. Appl. Phys. **94**, 4001 (2003).

³¹ We note that the theorem given in Ref. 30 does not prohibit the generation of spin-polarized current for devices with multi-channeled leads, which leaves possibilities of generation of spin-polarized current soley by gate in our DQW device experimentally. Research in this direction is underway.

³² B. K. Nikolić, P. Zarbo, and S. Souma, Chapter 24, page 814-866 in Volume I of The Oxford Handbook on Nanoscience and Technology (2010).

³³ M. Büttiker, Y. Imry, R. Landauer, and S. Pinhas, Phys. Rev. B **31**, 6207 (1985).

³⁴ T. Koga, T. Matsuura, S. Faniel, S. Souma, S. Mineshige, Y. Sekine, and H. Sugiyama, IEICE Trans. Electron. **E95-C**, 770 (2012).

³⁵ This value of a_{SO} was obtained by substituting the value $N_{\text{S}}^{\text{tot}} / 2$ to N_{S} in the formula $a_{\text{SO}} m_{||}^* / m_{\text{e}} = a - b N_{\text{S}}$ with $a = 1.46 \text{ e\AA}^2$ and $b = 1.51 \times 10^{-17} \text{ e\AA}^2 \text{ m}^2$ (see Ref. 28), where we used $m_{||}^* = 0.047 m_{\text{e}}$.

³⁶ The oscillation period presented here is an averaged value of more than 100 periods.

³⁷ Similarly, the disappearance of the rapid oscillation in G_{\uparrow} as it approaches to e^2/h is due to the disappearance of the wave function amplitude in QW2 at $x = L$ when $L = n\pi/2k'_{\alpha}$.